Soft Matter

A model for 3D deformation and reconstruction of contractile microtissues

Journal:	*Soft Matter*
Manuscript ID	SM-ART-06-2020-001182.R1
Article Type:	Paper
Date Submitted by the Author:	09-Oct-2020
Complete List of Authors:	Kim, Jaemin; Cornell University, MAE Mailand, Erik; Ecole Polytechnique Federale de Lausanne, Mechanical Engineering Ang, Ida; Cornell University, MAE Sakar, Mahmut Selman; Ecole Polytechnique Federale de Lausanne, Mechanical Engineering Bouklas, Nikolaos; Cornell University, MAE

Soft Matter

ARTICLE TYPE

Cite this: DOI: 00.0000/xxxxxxxxxx

A model for 3D deformation and reconstruction of contractile microtissues†

Jaemin Kim,[a] Erik Mailand,[b] Ida Ang,[a] Mahmut Selman Sakar,[b] and Nikolaos Bouklas[a]*

Received Date
Accepted Date

DOI: 00.0000/xxxxxxxxxx

Tissue morphogenesis and regeneration are essentially mechanical processes that involve coordination of cellular forces, production and structural remodeling of extracellular matrix (ECM), and cell migration. Discovering the principles of cell-ECM interactions and tissue-scale deformation in mechanically-loaded tissues is instrumental to the development of novel regenerative therapies. The combination of high-throughput three-dimensional (3D) culture systems and experimentally-validated computational models accelerate the study of these principles. In our previous work [E. Mailand *et al., Biophysical Journal*, 2019, **117**, 975-986], we showed that prominent surface stresses emerge in constrained fibroblast-populated collagen gels, driving the morphogenesis of fibrous microtissues. Here, we introduce an active material model that allows the embodiment of surface and bulk contractile stresses while maintaining the passive elasticity of the ECM in a 3D setting. Unlike existing models, the stresses are driven by mechanosensing and not by an externally applied signal. The mechanosensing component is incorporated in the model through a direct coupling of the local deformation state with the associated contractile force generation. Further, we propose a finite element implementation to account for large deformations, nonlinear active material response, and surface effects. Simulation results quantitatively capture complex shape changes during tissue formation and as a response to surgical disruption of tissue boundaries, allowing precise calibration of the parameters of the 3D model. The results of this study imply that in the organization of the extracellular matrix in the bulk of the tissue may not be a major factor behind the morphogenesis of fibrous tissues at sub-millimeter length scales.

1 Introduction

Mesenchymal and epithelial cells residing inside or on the surface of tissues apply traction forces to the matrix that they adhere to which lead to the remodeling of the fiber connections, cell migration, and bulk tissue deformation.[1–6] The physical interactions of the cells with the 3D interwoven network of fibers, ECM, influence their force output through the activity of mechanosensitive proteins.[7–9] Understanding the principles behind the cell-ECM interactions is important for various fields such as developmental biology and oncology, and controlling these interactions is instrumental for tissue engineering and regenerative medicine. Although technological and conceptual advances in the last decade built a solid foundation on epithelial tissue mechanics,[10–12] a detailed accounting of the dynamic stresses and strains that control the 3D architecture of fibrous tissues remain unclear.

The scientific impact and medical relevance of cell-ECM interactions has inspired the development of a repertoire of analytical and computational models where the focus has been recently on cellular mechanosensing and cell migration.[13–15] Physical models of cells, spanning from subcellular to supracellular scales, can be classified into three main categories: agent-based models, interfacial models, and continuum models.[16–20] Agent-based formulations such as vertex and Potts models have been widely used to capture the morphogenesis of epithelial monolayers.[21–24] Interfacial models including either sharp or diffuse formulations (e.g. phase-field model), treat tissues as viscous fluids by considering the energetics of internal and external interfaces. They are valid for tissues where there is no 3D structure based on an underlying ECM scaffold.[25–29] Continuum models, on the other hand, are better suited for 3D fibrous tissues because they describe the tissue as a bulk active material with a phenomenological constitutive law that enables the incorporation of cellular contractility and nonlinear properties of collagen networks such as mechanical

[a] *Sibley School of Mechanical and Aerospace Engineering, Cornell University, Ithaca, New York, USA.*
[b] *Institutes of Mechanical Engineering and Bioengineering, Ecole Polytechnique Fédérale de Lausanne, Lausanne, Switzerland.*
†Electronic Supplementary Information (ESI) available: See DOI: 00.0000/00000000.
* Corresponding Author. E-mail: nb589@cornell.edu (N. Bouklas).

anisotropy and time-dependent behavior.[30–36]

The majority of the existing continuum models for ECM-rich contractile microtissues are based on processing of signals as they use Hill's equations for contraction.[37] These equations were originally derived by Archibald Vivian Hill to model skeletal muscle contraction. Although cellular contractions triggered by neural or other external signals can be accurately captured by this formulation, tissue morphogenesis by fibroblasts or epithelial cells does not fall into this category. Furthermore, almost all models have simplified 2D geometries while cell residing in fibrous gels generate 3D stress and deformation fields. Another limitation of the existing models is that they do not capture the morphogenetic effects of cell migration.

Microfabricated tissues provide a controllable environment for investigating the effects of ECM mechanics, geometric constraints and external loading on tissue mechanics and cell behavior.[38–40] Data generated by these platforms have facilitated the development and validation of new computational models.[41–44] In our previous works, using microfabricated tissues and robotic manipulation, we showed that cell contractility at free surfaces is as critical as bulk contractility in shaping of fibroblast-populated collagen microtissues.[36,45] Surface effects are prominent in liquids but are often neglected in the continuum description of structural solids as they pertain to length scales that are mostly not relevant to engineered systems. In soft solids and gels, on the other hand, surface effects can have a significant influence in the overall mechanical response at physiologically relevant scales, and contribute to several phenomena including adhesion, fracture, and bulk deformation.[46–48] Recent advances in the continuum descriptions of surface effects in soft solids[49–51] and the development of corresponding numerical implementations in the finite element (FE) framework[52,53] have led to new insight in diverse areas, from instabilities in soft elastomers,[54] to diffusion kinetics in hydrogel microspheres loaded with drugs.[55] An implementation of surface elasticity at finite deformations is not directly available in commercial FE platforms such as ABAQUS, ANSYS and FEBio, thus, there is a demand for in-house implementations. Notably, elastocapillary effects arising from the interactions of surface elasticity with bulk elasticity lead to smoothing of sharp geometrical features in soft solids, a morphogenic event that cannot be captured by bulk effects represented in the traditional FE implementations.

We have recently introduced a 2D computational model of contractile tissues that couples passive elasticity of biological soft matter with active bulk and surface contractility.[36] The simulation results highlighted the unique contribution of modeling surface stresses for capturing tissue reconstruction upon external mechanical perturbations. However, 2D geometric representation restricted the surface effects to a line around the periphery of the tissue. Thus, the stresses on the top and bottom surfaces of the tissues were ignored. In reality, surface effects have to be considered over a 2D manifold that covers the entire surface of the 3D tissue to be accurately represented. To illustrate this deficiency, we can think of the following example. When the microtissues were detached from the constraining pillars, they contracted into a ball within 12 hours. A 2D model cannot capture the structural and morphological evolution of this event using planar stress and strain approximations. Even for morphological changes that essentially happen in a single plane, the comparison between experimental data and simulation results were restricted to qualitative assessment. It is instrumental to extend the theory and finite element implementation to 3D, which requires the introduction of more complex kinematics of surfaces. As surface and bulk contractile stresses are acting on the soft and highly compressible tissue, surface instabilities (e.g. wrinkling) may arise. We significantly modified the model of the ECM to allow for high compression without the emergence of surface instabilities.

In this work, we introduce an equilibrium continuum theory and corresponding finite element implementation that captures 3D morphological states of contractile microtissues. The proposed model is capable of reproducing complex 3D deformations resulting from the formation of microtissues and as a response to controlled mechanical loading as well as microsurgical operations. The model is not based on external signaling, and cell-ECM interactions are captured purely through mechanosensing. The mechanosensing component is incorporated in the model through a direct coupling of the local deformation state with the associated contractile force generation. In Section 2, we summarize the equilibrium theory capturing the interactions of cell and ECM in the bulk and on the surface of the microtissues along with the finite element implementation including the weak form and elasticity tensors. Section 3 describes experimental protocols including microtissue fabrication and robotic manipulation. Section 4 presents and discusses the simulations of tissue contraction and reconstruction.

2 Continuum mechanics framework

Fibroblasts accumulate at the periphery of reconstituted collagenous microtissues, which leads to formation of a heterogeneous architecture containing a collagen-rich core that is sparsely populated by cells and a fibronectin-rich shell with high fibroblast density.[36,56,57] Furthermore, when tissues are engineered inside rectangular wells, but subsequently released from the posts, they compact and attain a spherical shape in time.[36] The deviation from the rectangular shape that is defined by the geometry of the surrounding well is a clear indication that surface stresses govern the compaction process. Based on these observations, we postulated that the spatially heterogeneous force generation and shape reconfiguration can be represented in the continuum scale through the introduction of active surface stresses.[36] The model that we introduce in this section is based on mechanosensing of the local deformation state of the tissue. It has the potential to predict the stress distribution and the corresponding 3D deformation of microtissues by recapitulating the effects of multi-cellular organization and contractility. The resulting framework is a first step towards a model for ECM-rich active matter.

2.1 Key concepts in differential geometry

We briefly review key concepts of differential geometry required to describe the kinematics and equilibrium bulk and surface response. Hereafter, $\{\bullet\}$ and $\{\widehat{\bullet}\}$ denote bulk and surface quanti-

ties, respectively, for a body occupying volume Ω_0 bounded by outer surface denoted as $\partial\Omega_0$. It is important to note that a surface quantity to be introduced is not always equivalent with the bulk quantity evaluated on the surface.

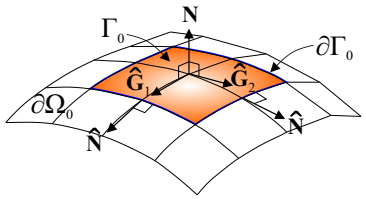

Fig. 1 General basis on a surface.

Let $\mathrm{d}\mathbf{R}$ denote an arbitrary infinitesimal vector expressed by general curvilinear coordinates, i.e., $\mathrm{d}\mathbf{R} = \mathrm{d}\mathbf{R}(\xi^1,\xi^2,\xi^3)$ in bulk, or $\mathrm{d}\mathbf{R} = \mathrm{d}\mathbf{R}(\hat{\xi}^1,\hat{\xi}^2)$ on the surface. We can always associate the general curvilinear coordinate with dual basis vectors by coordinate transformation.[52]

$$\mathbf{G}_i = \frac{\partial \mathbf{R}}{\partial \xi^i},\ \mathbf{G}^i = \frac{\partial \xi^i}{\partial \mathbf{R}} \quad \text{with} \quad \mathbf{I} = \delta^i_j\, \mathbf{G}_i \otimes \mathbf{G}^j \tag{1a}$$

$$\hat{\mathbf{G}}_\alpha = \frac{\partial \mathbf{R}}{\partial \hat{\xi}^\alpha},\ \hat{\mathbf{G}}^\alpha = \frac{\partial \hat{\xi}^\alpha}{\partial \mathbf{R}} \quad \text{with} \quad \hat{\mathbf{I}} = \delta^\alpha_\beta\, \hat{\mathbf{G}}_\alpha \otimes \hat{\mathbf{G}}^\beta \tag{1b}$$

where $\mathbf{G}_i$ (or $\hat{\mathbf{G}}_i$) and $\mathbf{G}^i$ (or $\hat{\mathbf{G}}^i$) are *covariant* and *contravariant* basis vectors, respectively. $\mathbf{I}$ is the unit tensor, and $\hat{\mathbf{I}} = \mathbf{I} - \mathbf{N}\otimes\mathbf{N}$ is the mixed surface unit tensor, where $\mathbf{N}$ is the outward unit normal vector. $\delta^i_j = \mathbf{G}^i \cdot \mathbf{G}_j$ and $\delta^\alpha_\beta = \hat{\mathbf{G}}^\alpha \cdot \hat{\mathbf{G}}_\beta$ are *Kronecker deltas* ($i,j = 1,2,3$, $\alpha,\beta = 1,2$).

The dual basis vectors are connected following

$$\mathbf{G}_i = G_{ij}\mathbf{G}^j \quad \text{and} \quad \mathbf{G}^i = G^{ij}\mathbf{G}_j \tag{2a}$$

$$\hat{\mathbf{G}}_\alpha = \hat{G}_{\alpha\beta}\hat{\mathbf{G}}^\beta \quad \text{and} \quad \hat{\mathbf{G}}^\alpha = \hat{G}^{\alpha\beta}\hat{\mathbf{G}}_\beta \tag{2b}$$

where G_{ij} (or $\hat{G}_{\alpha\beta}$) and G^{ij} (or $\hat{G}^{\alpha\beta}$) are *metric tensors*. Note that the mappings in Eq. 2 are inverse to each other, i.e. $[G_{ij}] = [G^{ij}]^{-1}$ and $[\hat{G}_{\alpha\beta}] = [\hat{G}^{\alpha\beta}]^{-1}$.

The gradient and divergence operators can be expressed in terms of basis vectors in the bulk and on the surface,

$$\mathrm{Grad}\{\bullet\} = \frac{\partial\{\bullet\}}{\partial \xi^i}\otimes\mathbf{G}_i \quad \text{and} \quad \mathrm{Div}\{\bullet\} = \frac{\partial\{\bullet\}}{\partial \xi^i}\cdot\mathbf{G}_i \tag{3a}$$

$$\widehat{\mathrm{Grad}}\{\hat{\bullet}\} = \frac{\partial\{\hat{\bullet}\}}{\partial \hat{\xi}^\alpha}\otimes\hat{\mathbf{G}}_\alpha \quad \text{and} \quad \widehat{\mathrm{Div}}\{\hat{\bullet}\} = \frac{\partial\{\hat{\bullet}\}}{\partial \hat{\xi}^\alpha}\cdot\hat{\mathbf{G}}_\alpha \tag{3b}$$

Let Γ_0 be a sub-surface on $\partial\Omega_0$ in Figure 1 ($\Gamma_0 \in \partial\Omega_0$), then the *divergence theorems* are defined by[49,58,59]

$$\int_{\Omega_0} \mathrm{Div}\{\bullet\}\,\mathrm{d}V = \int_{\partial\Omega_0} \{\bullet\}\cdot\mathbf{N}\,\mathrm{d}S \tag{4a}$$

$$\int_{\Gamma_0} \widehat{\mathrm{Div}}\{\hat{\bullet}\}\,\mathrm{d}S = \int_{\partial\Gamma_0} \{\hat{\bullet}\}\cdot\hat{\mathbf{N}}\,\mathrm{d}L - \int_{\Gamma_0} c\{\hat{\bullet}\}\cdot\mathbf{N}\,\mathrm{d}S \tag{4b}$$

where $\hat{\mathbf{N}}$ is the unit outward binormal vectors on the sub-surface boundary $\partial\Gamma_0$, as seen in Figure 1. Note that $c = -\widehat{\mathrm{Div}}\,\mathbf{N}$ is total curvature (twice the mean curvature, $c = 2\bar{c}$).[49,60]

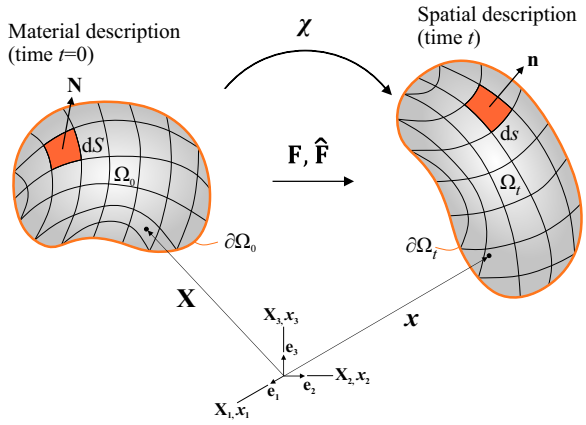

Fig. 2 Configuration and motion of a continuum body.

2.2 Kinematics

Let Ω_0 be a fixed reference configuration of a continuum body $\mathscr{B}$. We use the notation $\chi : \Omega_0 \to \mathbb{R}^3$ for the deformation of body $\mathscr{B}$. A motion χ is the vector field of the mapping $\boldsymbol{x} = \chi(\mathbf{X})$, of a material point in the reference configuration $\mathbf{X} \in \Omega_0$ to a position in the deformed configuration $\boldsymbol{x} \in \Omega$.

The kinematics of a typical particle are described by

$$\mathbf{u}(\mathbf{X},t) = \mathbf{x}(\mathbf{X},t) - \mathbf{X} \tag{5}$$

where $\mathbf{u}(\mathbf{X},t)$ is the displacement vector field in the spatial description.

The kinematics of an infinitesimal bulk element are described by

$$\mathbf{F}(\mathbf{X},t) = \frac{\partial \chi(\mathbf{X},t)}{\partial \mathbf{X}} = \mathrm{Grad}\boldsymbol{x}(\mathbf{X},t) = \mathbf{g}_i \otimes \mathbf{G}^i \tag{6a}$$

$$\mathbf{F}^{-1}(\boldsymbol{x},t) = \frac{\partial \chi^{-1}(\boldsymbol{x},t)}{\partial \boldsymbol{x}} = \mathrm{Grad}\mathbf{X}(\boldsymbol{x},t) = \mathbf{G}_i \otimes \mathbf{g}^i \tag{6b}$$

where $\mathbf{F}(\mathbf{X},t)$ and $\mathbf{F}^{-1}(\boldsymbol{x},t)$ are the deformation gradient and inverse deformation gradient, respectively. $\mathbf{G}_i$ (or $\mathbf{G}^i$) and $\mathbf{g}_i$ (or $\mathbf{g}^i$) are general curvilinear bases in the material and spatial configuration, respectively. Note that $J(\mathbf{X},t) = dv/dV = \det\mathbf{F}(\mathbf{X},t) > 0$ is the *Jacobian determinant* defining the ratio of a volume element between material and spatial configuration. We decompose the deformation gradient into a *volumetric* and an *isochoric* part.[61–63]

$$\mathbf{F} = (J^{1/3}\mathbf{I})\,\overline{\mathbf{F}} \tag{7}$$

where $J^{1/3}\mathbf{I}$ and $\overline{\mathbf{F}}$ represent the volumetric and isochoric parts of the deformation gradient $\mathbf{F}$. Following, we utilize $\{\overline{\bullet}\}$ to denote quantities associated with the isochoric part of the deformation gradient.

We introduce following *bulk* strain measures as follows:

$$\overline{\mathbf{C}} = \overline{\mathbf{F}}^{\mathrm{T}}\overline{\mathbf{F}} = J^{-2/3}\mathbf{C} = J^{-2/3}g_{ij}\mathbf{G}^i \otimes \mathbf{G}^j \tag{8a}$$

$$\overline{\mathbf{b}} = \overline{\mathbf{F}}\overline{\mathbf{F}}^{\mathrm{T}} = J^{-2/3}\mathbf{b} = J^{-2/3}G^{ij}\mathbf{g}_i \otimes \mathbf{g}_j \tag{8b}$$

$$\bar{I}_1 = \mathrm{tr}(\overline{\mathbf{C}}) = \mathrm{tr}(\overline{\mathbf{b}}) \tag{8c}$$

where $\overline{\mathbf{C}}$ and $\overline{\mathbf{b}}$ are the *modified right* and *left Cauchy-Green tensor*, and $\bar{I}_1$ is the modified first principal invariant.

In Figure 2, a unit normal vector $\mathbf{N}$ in the material configuration cannot be transformed into a unit normal vector $\mathbf{n}$ in the spatial configuration via the deformation gradient $\mathbf{F}$. This motivates us to develop the kinematics of an infinitesimal surface element,[49,64,65]

$$\widehat{\mathbf{F}}(\mathbf{X},t) = \frac{\partial \chi(\mathbf{X},t)}{\partial \mathbf{X}} \cdot \widehat{\mathbf{I}} = \widehat{\mathrm{Grad}}\boldsymbol{x}(\mathbf{X},t) = \widehat{\mathbf{g}}_\alpha \otimes \widehat{\mathbf{G}}^\alpha \tag{9a}$$

$$\widehat{\mathbf{F}}^{-1}(\boldsymbol{x},t) = \frac{\partial \chi^{-1}(\boldsymbol{x},t)}{\partial \boldsymbol{x}} \cdot \widehat{\boldsymbol{i}} = \widehat{\mathrm{Grad}}\mathbf{X}(\boldsymbol{x},t) = \widehat{\mathbf{G}}_\alpha \otimes \widehat{\mathbf{g}}^\alpha \tag{9b}$$

where $\widehat{\mathbf{F}}(\mathbf{X},t)$ and $\widehat{\mathbf{F}}^{-1}(\boldsymbol{x},t)$ are the surface deformation gradient and inverse surface deformation gradient, respectively. $\widehat{\mathbf{G}}_\alpha$ (or $\widehat{\mathbf{G}}^\alpha$) and $\widehat{\mathbf{g}}_\alpha$ (or $\widehat{\mathbf{g}}^\alpha$) are general surface curvilinear bases in the material and spatial configuration, respectively. $\widehat{\boldsymbol{i}} = \boldsymbol{i} - \mathbf{n}\otimes\mathbf{n}$ is the mixed surface unit tensor in spatial configuration and $\mathbf{i}$ is the unit tensor. It is important to note that $\widehat{\mathbf{F}}(\mathbf{X},t)$ is always a rank deficient tensor, thus *surface Jacobian determinant* should be indirectly obtained by $\widehat{J}(\mathbf{X},t) = da/dA = |\mathrm{cof}\,\mathbf{F}\cdot\mathbf{N}| > 0$.[49]

We introduce the *surface* strain measures as follows:

$$\widehat{\mathbf{C}} = \widehat{\mathbf{F}}^{\mathrm{T}}\widehat{\mathbf{F}} = \mathbf{C} : \widehat{\mathbf{I}} = \widehat{g}_{\alpha\beta}\widehat{\mathbf{G}}^\alpha \otimes \widehat{\mathbf{G}}^\beta \tag{10a}$$

$$\widehat{\mathbf{b}} = \widehat{\mathbf{F}}\widehat{\mathbf{F}}^{\mathrm{T}} = \mathbf{b} : \widehat{\mathbf{I}} = \widehat{G}^{\alpha\beta}\widehat{\mathbf{g}}_\alpha \otimes \widehat{\mathbf{g}}_\beta \tag{10b}$$

where $\widehat{\mathbf{C}}$ and $\widehat{\mathbf{b}}$ are *surface right* and *left Cauchy-Green tensors*.

2.3 Constitutive equations

In order to describe the equilibrium mechanical response of the microtissue we need to consider the "passive" ECM response, and the cell-induced "active" contraction which differs in the bulk and on the surface of the body. Thus we postulate the existence of a free-energy density function $\Psi(\mathbf{F})$ and a surface excess free energy density function $\widehat{\Psi}(\widehat{\mathbf{F}})$. Since we are developing an equilibrium theory, we postulate that the free energy density functions only depend on kinematic variables, assuming that cellular forces only depend on the affine deformations of the ECM.

We postulate that the free energy density can be decomposed into the passive and active parts as $\Psi(\mathbf{F}) = \Psi^p(J,\bar{I}_1) + \Psi^a(J)$. We assume that the ECM has a compressible hyperelastic response, and we use an additive decomposition of the passive free energy density into volumetric and isochoric contributions as $\Psi^p(J,\bar{I}_1) = \Psi^p_{vol}(J) + \Psi^p_{iso}(\bar{I}_1)$.[64–66] The surface excess free energy density function is assumed be constant per unit area in the spatial configuration, obtaining a fluid-like response.[36?] The two

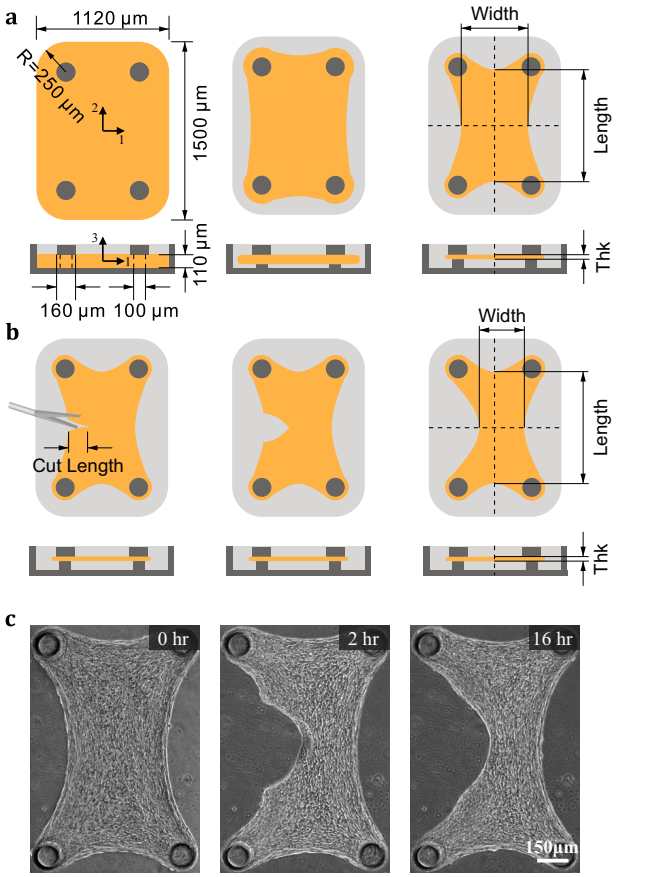

Fig. 3 Experimental model. (a) Schematic of initial (left), intermediate (center) and final (right) shapes during the course of microtissue formation. Microtissue evolution is shown from an in plane- (upper row) and out of plane- (lower row) perspective. A suspension of fibroblasts in collagen is spun down into rectangular microwells and allowed to gel, which self-assembles into microtissues constrained between flexible cantilevers. b) Schematic of surgical operation using microscissors mounted on the robotic system and subsequent microtissue shape evolution over time. c) Representative images showing the tissue before (left), 2 hours after (center), and 16 hours after the surgical operation.

expressions are

$$\Psi = \frac{\kappa}{2}(J-1)^2 + \frac{\mu}{2}(\bar{I}_1 - 3) + \eta J \tag{11a}$$

$$\widehat{\Psi} = \gamma\widehat{J} \tag{11b}$$

in which κ and μ are the bulk and shear moduli for passive bulk free energy density Ψ^p. The active bulk and surface free energy densities Ψ^a (last term in Eq. 11a) and $\widehat{\Psi}$ account for cellular contraction, where η and γ are the bulk and surface contractile moduli.[36,67]

Following the standard *Coleman-Noll procedure*[68,69] leads to constitutive equations for the *first Piola-Kirchhoff stress tensors* $\mathbf{P}$ in bulk and $\widehat{\mathbf{P}}$ on surface, given as

$$\mathbf{P} = \frac{\partial\Psi}{\partial\mathbf{F}} = Jp\mathbf{F}^{-T} + J^{-2/3}\mathbf{F}(\mathbb{P} : \overline{\mathbf{S}}) + \eta J\mathbf{F}^{-T} \tag{12a}$$

$$\widehat{\mathbf{P}} = \frac{\partial\widehat{\Psi}}{\partial\widehat{\mathbf{F}}} = \gamma\widehat{J}\widehat{\mathbf{F}}^{-T} \tag{12b}$$

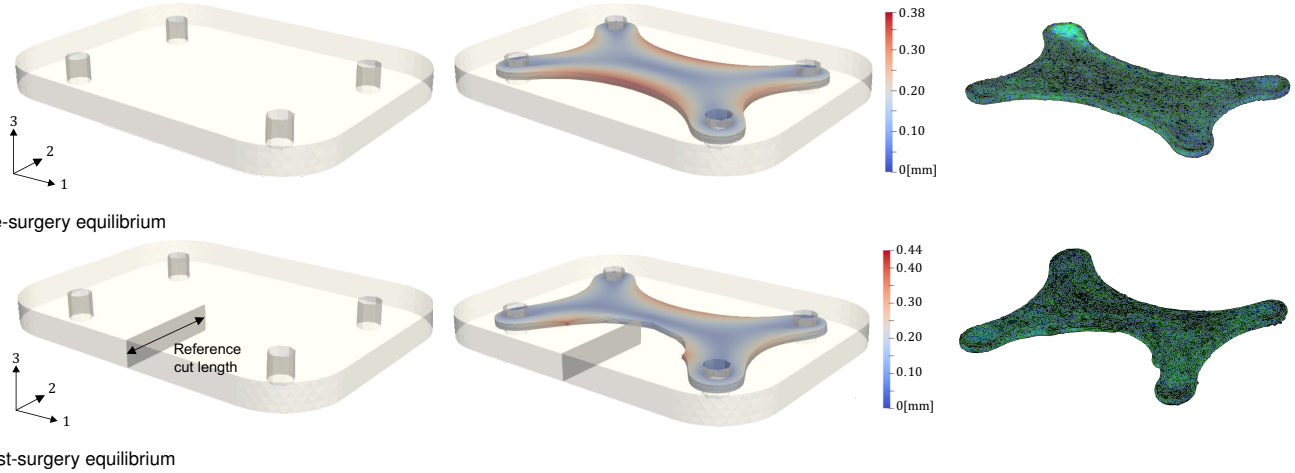

Fig. 4 3D images of simulated and experimentally-visualized microtissues. (a) Undeformed (*left*) and equilibrium configuration (*middle*) from the finite element simulations along with the pre-surgery equilibrium shape of the microtissue (*right*). (b) Undeformed with the projected cut (*left*) and equilibrium configuration (*middle*) from the finite element simulations along with the post-surgery equilibrium shape of the microtissue (*right*).

with the constitutive equations for the *hydrostatic pressure* p and the *fictitious second Piola-Kirchhoff stress* $\overline{\mathbf{S}}$

$$p = \frac{\mathrm{d}\Psi_{vol}}{\mathrm{d}J} \tag{12c}$$

$$\overline{\mathbf{S}} = 2\frac{\partial \Psi_{iso}}{\partial \overline{\mathbf{C}}} \tag{12d}$$

where $\mathbb{P} = \mathbb{I} - (1/3)\mathbf{C}^{-1} \otimes \mathbf{C}$ is a fourth order projection tensor.[65]

2.4 Equilibrium

The total potential energy functional $I(\chi)$ is defined as:

$$I(\chi) = \int_{\Omega_0} \Psi(\mathbf{F},\chi;\mathbf{X})\mathrm{d}V + \int_{\partial\Omega_0} \widehat{\Psi}(\widehat{\mathbf{F}},\chi;\mathbf{X})\mathrm{d}S \tag{13}$$
$$- \int_{\Omega_0} \mathbf{B}\cdot\mathbf{u}(\chi;\mathbf{X})\,\mathrm{d}V - \int_{\partial\Omega_0} \mathbf{T}\cdot\mathbf{u}(\chi;\mathbf{X})\,\mathrm{d}S$$

where $\mathbf{B}$ is the reference body force and $\mathbf{T}$ is the surface traction. An equilibrated configuration is obtained by minimizing this functional considering all admissible deformations $\delta\chi$.

Following the derivation presented in Javili *et al.* (2010),[?] we can finally arrive at a set of localized force balance equations. Neglecting the inertial effect, the local form of linear and angular momentum balances for bulk[64,65] and surface[49,60] are defined by

$$\mathrm{Div}\,\mathbf{P} + \mathbf{B} = \mathbf{0} \quad \text{and} \quad \mathbf{F}\mathbf{P}^{\mathrm{T}} = \mathbf{P}\mathbf{F}^{\mathrm{T}} \quad \text{in } \Omega \tag{14a}$$

$$\widehat{\mathrm{Div}}\,\widehat{\mathbf{P}} + \mathbf{T} - \mathbf{P}\mathbf{N} = \mathbf{0} \quad \text{and} \quad \widehat{\mathbf{F}}\widehat{\mathbf{P}}^{\mathrm{T}} = \widehat{\mathbf{P}}\widehat{\mathbf{F}}^{\mathrm{T}} \quad \text{on } \partial\Omega \tag{14b}$$

Note that a Neumann-type boundary condition is also defined on boundary curves $\partial\Gamma_0$ as, $[\![\widehat{\mathbf{P}}\cdot\widehat{\mathbf{N}}]\!] = 0$, where the double bracket indicates summation over surfaces intersecting on boundary curves.[52] The standard Neumann boundary condition can be obtained if the term involving surface stress is neglected. In this work we assume that the surface excess free energy does not depend on the orientation of the surface itself, namely there is no functional dependence of $\widehat{\Psi}$ on the normal vector $\mathbf{N}$ on the surface $\partial\Omega$.

2.5 Elasticity tensors

Iterative solution techniques are employed to solve the proposed nonlinear problem.[70] We here present the analytical expression of the *elasticity tensors* for the linearization of the constitutive equations. The elasticity tensors $\mathbb{C} = \mathbb{C}^p_{vol} + \mathbb{C}^p_{iso} + \mathbb{C}^a$ in the bulk and $\widehat{\mathbb{C}}$ on the surface are defined by

$$\mathbb{C}^p_{vol} = J\tilde{p}\mathbf{C}^{-1}\otimes\mathbf{C}^{-1} - 2Jp\mathbf{C}^{-1}\odot\mathbf{C}^{-1} \tag{15a}$$

$$\mathbb{C}^p_{iso} = \mathbb{P}:\overline{\mathbb{C}}:\mathbb{P}^{\mathrm{T}} + \frac{2}{3}\mathrm{Tr}(J^{-2/3}\overline{\mathbf{S}})\tilde{\mathbb{P}}$$
$$- \frac{2}{3}(\mathbf{C}^{-1}\otimes\mathbf{S}_{iso} + \mathbf{S}_{iso}\otimes\mathbf{C}^{-1}) \tag{15b}$$

$$\mathbb{C}^a = J\eta\mathbf{C}^{-1}\otimes\mathbf{C}^{-1} - 2J\eta\mathbf{C}^{-1}\odot\mathbf{C}^{-1} \tag{15c}$$

$$\widehat{\mathbb{C}} = \widehat{J}\gamma\widehat{\mathbf{C}}^{-1}\otimes\widehat{\mathbf{C}}^{-1} - 2\widehat{J}\gamma\widehat{\mathbf{C}}^{-1}\odot\widehat{\mathbf{C}}^{-1} \tag{15d}$$

where the symbols are introduced for short-hand notations,[65]

$$\tilde{p} = p + J\frac{\mathrm{d}p}{\mathrm{d}J}, \quad \overline{\mathbb{C}} = 4J^{-4/3}\frac{\partial^2\Psi_{iso}}{\partial\overline{\mathbf{C}}\partial\overline{\mathbf{C}}}, \quad \mathbf{S}_{iso} = \frac{\partial\Psi_{iso}}{\partial\mathbf{C}} \tag{16a}$$

$$\mathbf{C}^{-1}\odot\mathbf{C}^{-1} = -\frac{\partial\mathbf{C}^{-1}}{\partial\mathbf{C}}, \quad \widehat{\mathbf{C}}^{-1}\odot\widehat{\mathbf{C}}^{-1} = -\frac{\partial\widehat{\mathbf{C}}^{-1}}{\partial\widehat{\mathbf{C}}} \tag{16b}$$

$$\tilde{\mathbb{P}} = \mathbf{C}^{-1}\odot\mathbf{C}^{-1} - \frac{1}{3}\mathbf{C}^{-1}\otimes\mathbf{C}^{-1}, \quad \mathrm{Tr}(\bullet) = (\bullet):\mathbf{C} \tag{16c}$$

2.6 Weak form

For the finite element implementation, we need to obtain the weak form for our problem.[71] By adding the constraint that the first variation of the total potential energy must be equal to zero

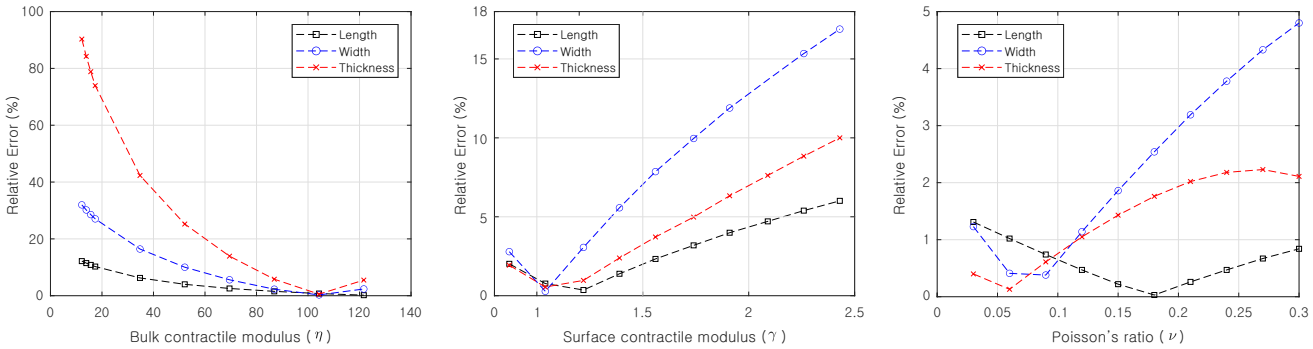

(a) pre-surgery equilibrium

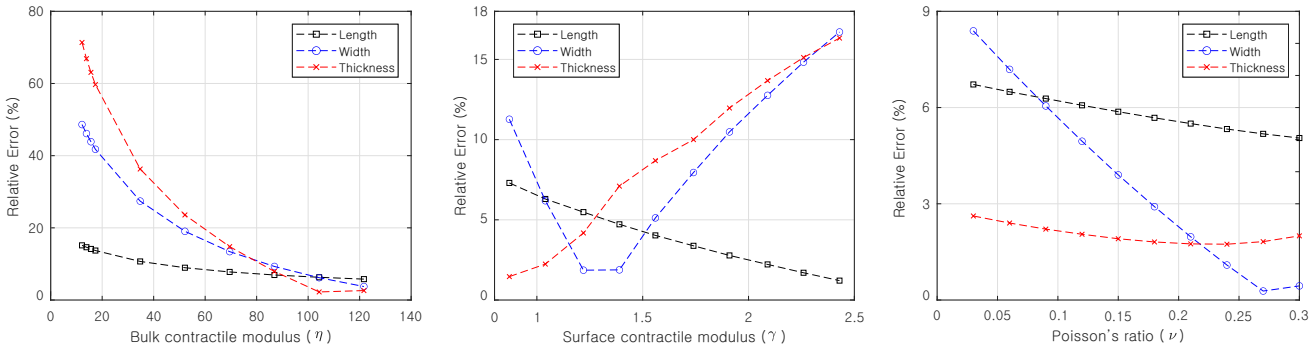

(b) post-surgery equilibrium

Fig. 5 Error analysis. Relative error for the equilibrium tissue dimensions between simulated values and experimental data as a function of bulk (*left*) and surface contractile moduli (*middle*), and Poisson's ratio (*right*)

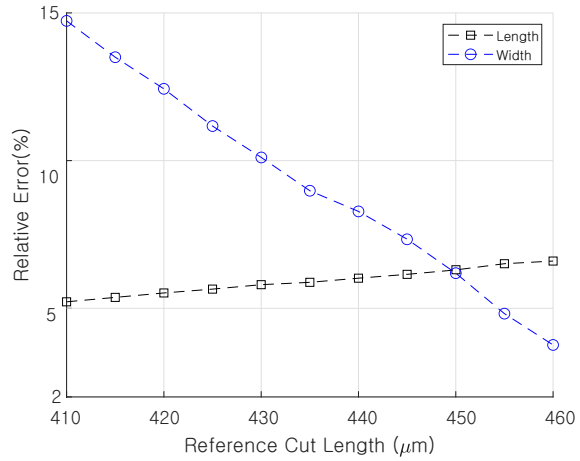

Fig. 6 Mapping evaluation of reference cut length (See Figures 3 and 4 for the measurement of the current and reference cut length, respectively)

$\delta I(\chi) = 0$, we obtain a weak form statement as

$$G = \int_{\Omega_0} \mathbf{P} : \mathrm{Grad}\delta\mathbf{u}\, \mathrm{d}V + \int_{\partial\Omega_0} \widehat{\mathbf{P}} : \widehat{\mathrm{Grad}}\delta\mathbf{u}\, \mathrm{d}S$$
$$- \int_{\Omega_0} \mathbf{B}\cdot\delta\mathbf{u}\, \mathrm{d}V - \int_{\partial\Omega_0} \mathbf{T}\cdot\delta\mathbf{u}\, \mathrm{d}S = 0 \quad \forall\, \delta\mathbf{u} \qquad (17)$$

where $\delta\mathbf{u}$ is the admissible deformation field. Note that the first and second lines of Eq. 17 are related with internal and external virtual work, respectively.

We employed the open-source platform FEniCS,[72,73] to implement the finite element simulation. We used the Scalable Nonlinear Equations Solvers (SNES) from the open-source toolkit PETSc,[74] which provides numerical computations of a *Newton-type* iterative procedure to solve the nonlinear variational problem. Note that the values of η and γ should be ramped from zero to their prescribed values for numerical stability.

3 Experiment method

3.1 Cell culture

NIH-3T3 fibroblasts (Sigma-Aldrich) were cultured in Dulbecco's modified Eagle's medium GlutaMAX (Life Technologies, Carlsbad, CA) supplemented with 10% fetal bovine serum (Life Technologies) and 1% penicillin-streptomycin (Life Technologies). Cells were passaged every 2-3 days using Trypsin 0.25% EDTA (Life Technologies) up to 20 times. All experiments were done with cells that tested negative for mycoplasma.

3.2 Microtissue model

Microtissue devices were fabricated as described elsewhere.[41,45] Briefly, Polydimethylsiloxane (PDMS, Sylgard 184, Dow-Corning) substrates were moulded from SU-8 masters. Prior to cell seeding, devices were treated with Pluronic-F127 (Sigma-Aldrich) for 15 minutes at room temperature to prevent adhesion. One million cells were suspended in 2 mgml-1 collagen type I from rat tail (Corning BV Life Sciences) and the suspension was added into the microfabricated device. The assembly was centrifuged to drive cells into the microwells containing the cantilevers. After removal of excess solution, the device was centrifuged once more

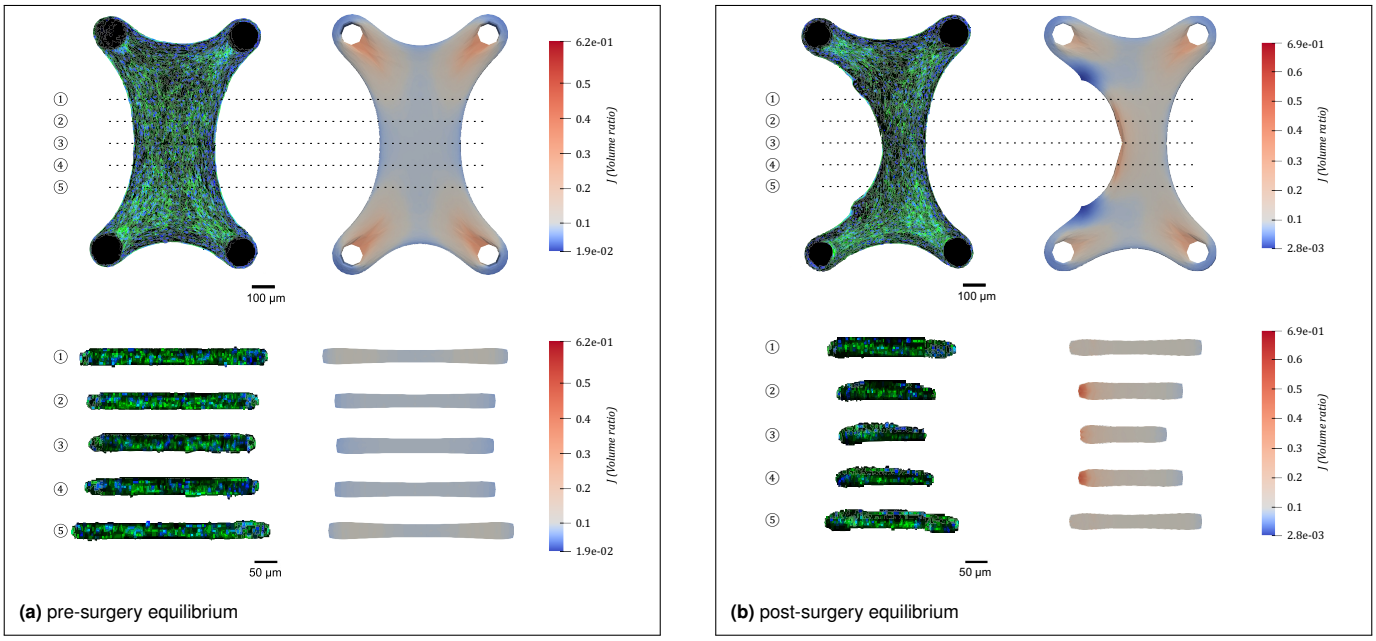

Fig. 7 Comparison between experimental data and simulation results for the (a) pre-surgery and (b) post-surgery equilibrium states. Top view (*top*) and cross-sectional views (*bottom*) are presented for each state. Cross-sections are equally spaced by 100μm from the center of the tissue. Contour plots from simulations show the volume ratio J, which is proportional to the inverse of the density of the tissue.

but upside down to drive cells to the height of the cantilever caps. A few hours after polymerisation, the collagen matrix compacted due to cellular contractility while the cantilevers constrain the direction of compaction.

3.3 Robotic micromanipulation

Surgical operations[75,76] were performed as described previously.[36] Briefly, microscissors (Alcon) were attached to a teleoperated robot that consists of six piezoelectric stick-slip actuators for each translation and rotation axis, and a 3D-printed tool adaptor. The robot was mounted on a motorized inverted microscope (Nikon Ti Eclipse) microscope for visualization. A stepper motor (Haydon Kerk Pittman) controlled by an Arduino microprocessor actuates the tools.

3.4 Microscopy and quantitative image analysis

Wide field imaging was done on a motorized inverted microscope (Nikon Ti Eclipse) microscope equipped with a live-cell incubator (Life Imaging Services). Phase-contrast images were captured with an ORCA-Flash4.0 digital CMOS camera (Hamamatsu) and a Plan Fluor 10x objective. For 3D imaging, microtissues were fixed with 4% formaldehyde and permeabilized with 0.2% Triton X-100, Immunostatining was performed for the nuclei and F-actin with Hoechst 33342 (Thermo Fisher Scientific) and Phalloidin, respectively. Labelled microtissues were imaged using a laser scanning confocal microscope (LSM 700, Zeiss) equipped with a 20x objective. 3D reconstruction of acquired images was done in ImageJ (NIH). The dimensions of the tissues were measured from the confocal images using an image processing script written in ImageJ.

4 Results and discussion

We engineered arrays of microtissues from fibroblasts suspended in reconstituted collagen solution using a high-throughput microfabricated device. Elastomer pillars located in each well constrain the microtissues, enabling long-term recording and repeatable robotic micromanipulation. The configuration of the tissues right after crosslinking of the cell-ECM suspension inside the wells (Figure 3a, left) was taken as the reference (undeformed) state for the material model. Over the course of 24 hours, forces applied by the encapsulated fibroblasts compacted the gel until reaching an equilibrium state. (Figure 3a, right). It is worth noting that the tissues continued to contract after the first 24 hours but with a significantly lower rate. We operated on a subset of microtissues that were in their equilibrium state, which we call pre-surgery equilibrium to avoid confusion, using a robotic micromanipulation system. The operation generated a clean cut with well-defined length and position on one of the longer sides of the microtissues (Figure 3b). The cut leaves two convex edges due to the disruption of collagen fibers at the surgery site. In the following hours, the damaged contour gradually transformed into a smooth concave edge, with a single curvature that was higher than that of the opposing side of the tissue. The reconstruction process resulted in a new equilibrium state after 16 hours (Figure 3c), which we call post-surgery equilibrium. The geometrical dimensions are illustrated in Figure 3.

We acquired stacks of images of fluorescently labeled microtissues using confocal microscopy to quantify their 3D shape. The cells cover all the space including the surfaces, therefore staining filamentous actin and nuclei were sufficient to capture the overall shape. The high-throughput device provides almost identical boundary conditions for every tissue. However, the wells

	Width (μm)		Thickness (μm)	
	Experiment	Simulation	Experiment	Simulation
①	420	433	37	38
②	384	384	37	37
③	371	370	37	36
④	385	385	37	37
⑤	436	433	37	38

(a) pre-surgery equilibrium

	Width (μm)		Thickness (μm)	
	Experiment	Simulation	Experiment	Simulation
①	293	312	38	37
②	224	244	40	40
③	196	208	44	45
④	218	244	41	40
⑤	295	312	38	37

(b) post-surgery equilibrium

Table 1 Measured and calculated values of the width and thickness of the microtissue shown in Figure 7 for the pre-surgery and post-surgery equilibrium states

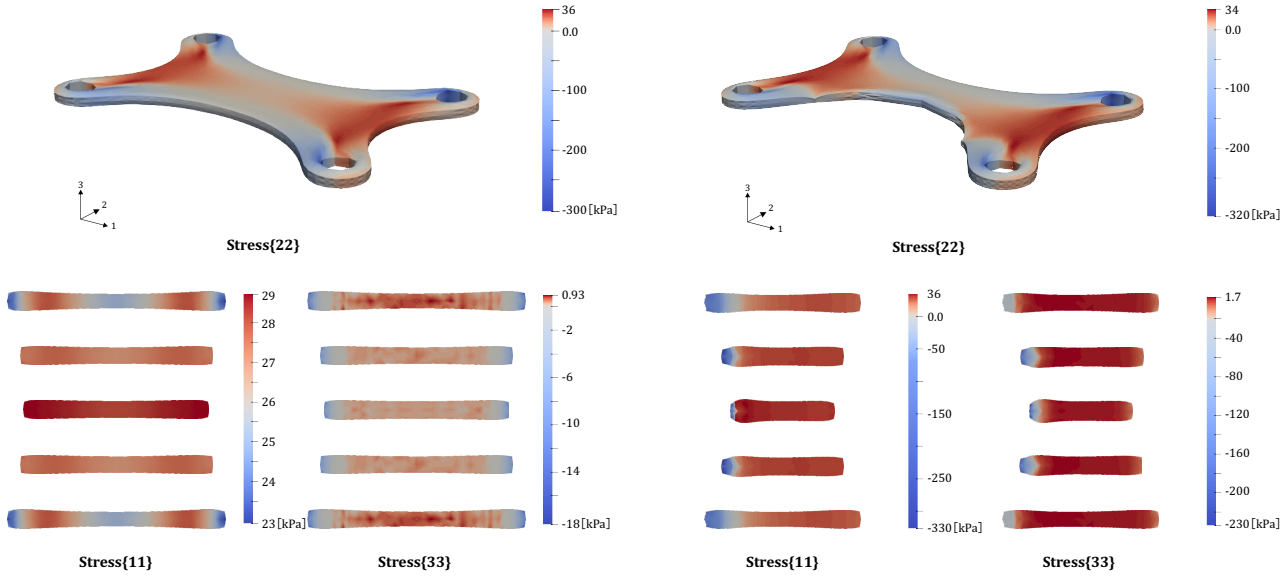

(a) pre-surgery equilibrium **(b)** post-surgery equilibrium

Fig. 8 Finite element simulations of the normal components of the first Piola-Kirchhoff stress tensor for (a) the pre-surgery and (b) the post-surgery equilibrium states. Top view (*top*) and sectional views (*bottom*) are presented for each state. Cross-sections are equally spaced by 100μm from the center of the tissue.

are small enough to observe macroscopic differences in tissue shape due to statistical deviations in the initial conditions such as cell number, distribution of cells inside the gel, and gel composition. As a result, the cross-sectional area of the microtissues at their equilibrium states varied by $10 \pm 2\%$. This variation is in accordance with published work on microtissues engineered using similar devices.[56,77] The cell-laden collagen gel compacted significantly until reaching the equilibrium shape. The surface area (width x length) of the tissues at the pre-surgery equilibrium state was $\approx 25\%$ of their reference state. Notably, out-of-plane deformation was even higher reaching $\approx 90\%$ in cross-sectional area (thickness x width), reinforcing the necessity of 3D modelling.

The computational model is derived from an equilibrium theory and therefore it cannot capture the transient states of the morphogenetic process. The parameters were calibrated with respect to the experimental measurements of a representative microtissue at its pre-surgery equilibrium. Using these calibrated parameters, we validated our model by comparing simulation results with the empirical data coming from post-surgery equilibrium state of the same representative microtissue. Bulk and surface contractile moduli, η and γ, drive the contractile response in the simulations while no external mechanical force was applied to the system. The only other forces acting on the tissue were the reaction forces generated at the cantilevers, where frictionless contact was assumed for the simulation. Therefore, when η and γ are set to zero, the material is considered to be in a stress-free state, as shown in Figure 4a(left) and b(left). In this undeformed state, which corresponds to the reference state in the experiments, bulk and surface free energy are equal to zero. For numerical stability reasons, the values of η and γ were gradually increased from zero to their prescribed values during the incremental nonlinear analysis. When the contractile moduli η and γ reach their prescribed values, the material is considered to be at an equilibrium state Figure 4a(middle) and b(middle). Experimentally, this corresponds to the equilibrium state of the microtissues, shown in Figure 4a(right) and b(right), respectively. To obtain the post-

surgery equilibrium from the finite element simulation a cut has to be introduced in the domain fig. 3b(left), which can be mapped back to the undeformed state Figure 4b(left) in a straightforward way that will be explained in Section 4.2.

4.1 Calibration of material properties

The parameters of the model are the bulk and shear moduli, κ and μ, and bulk and surface contractile moduli, η and γ. Following the literature[36] we set the value of shear modulus at $\mu = 8$ kPa. There is a unique relationship between μ, κ, and Poisson's ratio ν, allowing to interchangeably use ν in place of κ for the calibration procedure. We calibrated ν, η and γ through an error analysis between the simulation and experimental results on the pre-surgery equilibrium (Figure 5a) using the tissue dimensions defined in Figure 3 as the metric.

We selected the set of parameters that minimized the error for the length, width and thickness at the pre-surgery equilibrium, setting $\nu = 0.09$ ($\kappa = 7$ kPa), $\eta = 104.28$ kPa and $\gamma = 1.04$ mN/mm. The corresponding Young's modulus was calculated as $E = 17.38$ kPa, which is within the range of values reported on similar experimental models of microtissues.[41,78] We performed a similar calibration on the 2D model of the microtissue elsewhere.[36] Notably, while the value of γ is close to the reported one, η is an order of magnitude larger compared to the results of the 2D calibration. As a matter of fact, active bulk contraction was the main driver for the out-of-plane tissue deformation as seen in Figure 5a. The large 3D compaction, that our model captured, resulted in a ν value from the calibration procedure that indicates compressibility of the collagen matrix higher than previously assumed in computational models.[41,78]

Parameter values were validated through a second set of error analysis, this time taking the post-surgery equilibrium state as the output. The results of the error analysis are presented in Figure 5b. We obtained a deviation less than 10% for all the tissue dimensions. While the calibrated values of η and γ also minimize the error, the calibrated value of ν did not provide optimal results for the post-surgery equilibrium. We hypothesize that this deviation is due to the changes in the local tissue composition during the reconstruction process, since surgical manipulation creates a new boundary around which cells can migrate and tow ECM components.[36]

4.2 Recapitulating the surgical cut in the model

The length of the microsurgical cut at the pre-surgery equilibrium in Figure 3b(left) state must be projected to the reference state to perform simulations of the post-surgery equilibrium response. This projection resulted in a referential cut length of Figure 4b(left) 450 μm, which is utilized to prescribe a cut in the geometry discretized for the finite element simulation Figure 4b(middle). A series of simulations were performed for the post-surgery equilibrium response at different reference cut lengths to test the sensitivity of the results. As shown in Figure 6, deviation curves in both length and width cross at a point near 450 μm, which is consistent with the initial calculation based on the empirical data.

4.3 3D deformation and reconstruction

The proposed model recapitulates the extreme deformations of 3D microtissues in both pre-surgery and post-surgery equilibria, as shown in Figure 7. Accurate predictions for the cross-sectional shapes were obtained at all positions and in both equilibrium states. A one-to-one quantitative comparison of the cross-sectional dimensions are shown in Table 1. The highest discrepancy was observed at the post-surgery equilibrium state in the middle cross-sectional view (Figure 7b), as the experimental profile is not symmetric about the x_2 axis, which could be due an asymmetric microsurgical cut.

The theoretical formulation predicts that the bulk and surface contractile moduli lead to i) minimization of body volume and ii) reduction of surface area and smoothing of features with high curvatures, respectively. These deformations will be resisted by the bulk passive elasticity. However, the geometrical constraints, induce a conflict between the bulk contraction and surface effects during the shape evolution. This occurs as bulk contraction creates four concave sides as seen in the top-view in fig. 7a(top), but surface stresses oppose this trying to minimize curvature.

The model reports mechanical stresses throughout the tissues at their equilibrium states, as shown in Figure 8. The in-plane stresses calculated for the pre-surgery equilibrium state are qualitatively comparable with the predictions of analogous 2D models,[36,41] including the alignment of the principal stress and the generation of large gradients of intratissue stresses that originate from the cantilevers. The relatively high compressive values of in-plane normal stresses (P_{11} and P_{22} in Figure 8) correlate with areas of high cell density in Figure 7 (top), an observation that must be quantitatively evaluated in the future. In-plane normal stresses are more prominent around the cantilevers and in the periphery of the tissue. These observations suggest that the elongated cells at the tissue boundaries, which were shown to align along the principal stretch direction, exhibit high contractility. The stress redistribution in the post-surgery equilibrium state is intrinsically coupled with the processes of forming a smooth continuous concave edge. In the case where surface active elasticity was not considered, the edges of the cut would remain sharp as shown in our previous work.[36] Significant stress redistribution is also observed in the cross-sectional views along the x_2x_3 plane (P_{11} and P_{33} in Figure 8) where a symmetric profile seen in the pre-surgery equilibrium changes to an asymmetric shape at the post-surgery equilibrium.

4.4 Mechanical response

We estimated the contractile force of 3D microtissues at the pre-surgery equilibrium state by measuring the reaction forces on the cantilevers using the same material parameters as described in Section 4.1. The total reaction force on the four cantilevers were calculated to be 18.4 μN, which is on the same order of magnitude as experimentally reported values.[44,77,79,80] In these studies, the contractile forces were measured using cantilever deflection and linear beam theory, and the reported values were between 15 μN and 35 μN.

Unlike models that follow Hill's contractility law or models pre-

sented in[81] and[14], our model is based on an equilibrium theory and does not consider the transient response with an explicit dynamic reciprocity between cells and the surrounding ECM. This inherent difference allows our model to directly capture the steady state that results from the mechanosensing feedback loop. The contributions of active bulk and surface contraction to the potential energy in Eq. 11 are ηJ and $\gamma\widehat{J}$. These terms act to minimize J and $\widehat{J}$, which represent the activity of the cells in the bulk and on the surface, respectively. This activity counteracts the tendency of the ECM, represented by the passive part of the bulk free energy, to maintain the undeformed shape of the tissue (i.e. $J=1$ and $\widehat{J}=1$). The equilibrium between the active and passive terms represents the steady state that is a manifestation of the mechanosensing feedback loop.

5 Conclusions

Building on our previous work,[36] which demonstrated that the active surface effects are essential for modeling the complex deformation patterns in 2D microtissue shaping and response to injury, we presented a continuum-based model for 3D deformation and reconstruction of fibrous tissues that implemented distinct cell-ECM interactions in the bulk and on the surface of the material. This model provides a theoretical and computational framework in which the tissue-level mechanical response is governed by a set of constitutive and governing equations. 3D simulation results closely match the complex shape changes of microtissues in response to surgical manipulation, an operation that resembles fracture. The 3D model was calibrated against the aforementioned experiments leading to a set of physically meaningful parameters increasing the fidelity of the simulation results compared to the less physically meaningful 2D approximation.

Our results show that the the combination of bulk and surface contraction are sufficient for predicting the equilibrium shapes for tissue formation and reconfiguration. Notably, quantification of the material properties and reaction forces suggest that cells display non-uniform contractile responses during the reconstruction process. Current calibration process is based on the initial cell density and does not explicitly considers the spatial variation of cells due to migration.

Active surface effects may arise from a number of microscopic events that influence cell/ECM interactions, including cell migration, near-surface ECM remodeling, and changes in the cellular architecture due to geometry (e.g., stress fiber formation in cells spreading on surfaces). The accuracy of our simulation results demonstrates that incorporating active surface effects in the model is sufficient to capture the 3D tissue morphogenesis in our in vitro model. The current version of the computational model considers isotropic passive and active contributions, neglecting the effect of fiber remodeling and ECM plasticity, topics that have been extensively studied in the literature. The accuracy of our predictions alludes to the fact that these processes may be secondary in the bulk shaping and reconstruction processes at the given length scales, with "active" elastocapillary effects being the dominating factor. Structural changes inside and around the tissue may play an important role in the build up of the surface stresses, an important question that will be explored in our future work. Notably, surface effects are size dependent, thus, they are expected to play a much lesser role at larger length scales.

It would be also interesting to extend the model to consider changes in the initial cell density and adapt the functional forms of the surface and bulk contractile moduli to react to changes in cell density. The authors also plan to incorporate fiber realignment and network reconfiguration/plasticity into the model. Ultimately, we plan to model cell migration as a continuum field by deriving a mechanosensitive cell kinetics law.

Conflicts of interest

There are no conflicts to declare.

Acknowledgements

E.M. and M.S.S. acknowledge support from the European Research Council (ERC) under the European Union's Horizon 2020 research and innovation program (Grant agreement No. 714609).

References

1 J. A. Pedersen and M. A. Swartz, *Annals of biomedical engineering*, 2005, **33**, 1469–1490.
2 S. Even-Ram and K. M. Yamada, *Current opinion in cell biology*, 2005, **17**, 524–532.
3 F. Grinnell and W. M. Petroll, *Annual review of cell and developmental biology*, 2010, **26**, 335–361.
4 T. Mammoto and D. E. Ingber, *Development*, 2010, **137**, 1407–1420.
5 J. Foolen, T. Yamashita and P. Kollmannsberger, *Journal of Physics D: Applied Physics*, 2015, **49**, 053001.
6 S. Van Helvert, C. Storm and P. Friedl, *Nature cell biology*, 2018, **20**, 8.
7 J. Eyckmans, T. Boudou, X. Yu and C. S. Chen, *Developmental cell*, 2011, **21**, 35–47.
8 B. D. Hoffman, C. Grashoff and M. A. Schwartz, *Nature*, 2011, **475**, 316–323.
9 V. Vogel, *Annual review of physiology*, 2018, **80**, 353–387.
10 C. Guillot and T. Lecuit, *Science*, 2013, **340**, 1185–1189.
11 B. Ladoux and R.-M. Mège, *Nature Reviews Molecular Cell Biology*, 2017, **18**, 743.
12 W. Xi, T. B. Saw, D. Delacour, C. T. Lim and B. Ladoux, *Nature Reviews Materials*, 2019, **4**, 23–44.
13 B. Cheng, M. Lin, G. Huang, Y. Li, B. Ji, G. M. Genin, V. S. Deshpande, T. J. Lu and F. Xu, *Physics of life reviews*, 2017, **22**, 88–119.
14 H. Ahmadzadeh, M. R. Webster, R. Behera, A. M. J. Valencia, D. Wirtz, A. T. Weeraratna and V. B. Shenoy, *Proceedings of the National Academy of Sciences*, 2017, **114**, E1617–E1626.
15 M.-C. Kim, Y. R. Silberberg, R. Abeyaratne, R. D. Kamm and H. H. Asada, *Proceedings of the National Academy of Sciences*, 2018, **115**, E390–E399.
16 P. Kollmannsberger, C. Bidan, J. Dunlop and P. Fratzl, *Soft matter*, 2011, **7**, 9549–9560.

17 M. A. Wyczalkowski, Z. Chen, B. A. Filas, V. D. Varner and L. A. Taber, *Birth defects research part C: Embryo today: Reviews*, 2012, **96**, 132–152.

18 A. G. Fletcher, F. Cooper and R. E. Baker, *Philosophical Transactions of the Royal Society B: Biological Sciences*, 2017, **372**, 20150519.

19 R. Alert and X. Trepat, *Annual Review of Condensed Matter Physics*, 2019, **11**, year.

20 M. R. Shaebani, A. Wysocki, R. G. Winkler, G. Gompper and H. Rieger, *Nature Reviews Physics*, 2020, 1–19.

21 A. F. Marée, V. A. Grieneisen and P. Hogeweg, *Single-cell-based models in biology and medicine*, Springer, 2007, pp. 107–136.

22 A. G. Fletcher, M. Osterfield, R. E. Baker and S. Y. Shvartsman, *Biophysical journal*, 2014, **106**, 2291–2304.

23 N. Murisic, V. Hakim, I. G. Kevrekidis, S. Y. Shvartsman and B. Audoly, *Biophysical journal*, 2015, **109**, 154–163.

24 S. Alt, P. Ganguly and G. Salbreux, *Philosophical Transactions of the Royal Society B: Biological Sciences*, 2017, **372**, 20150520.

25 G. Forgacs, S. Newman, Z. Polikova and A. Neumann, *Colloids and Surfaces B: Biointerfaces*, 1994, **3**, 139–146.

26 S. Osher and R. P. Fedkiw, *Journal of Computational physics*, 2001, **169**, 463–502.

27 E. Javierre, F. Vermolen, C. Vuik and S. Van der Zwaag, *Journal of mathematical biology*, 2009, **59**, 605–630.

28 M. L. Manning, R. A. Foty, M. S. Steinberg and E.-M. Schoetz, *Proceedings of the National Academy of Sciences*, 2010, **107**, 12517–12522.

29 J. C. Arciero, Q. Mi, M. F. Branca, D. J. Hackam and D. Swigon, *Biophysical journal*, 2011, **100**, 535–543.

30 J. E. Bischoff, E. M. Arruda and K. Grosh, *Biomechanics and modeling in mechanobiology*, 2004, **3**, 56–65.

31 H. Tang, M. J. Buehler and B. Moran, *Annals of biomedical engineering*, 2009, **37**, 1117–1130.

32 D. Ambrosi, G. A. Ateshian, E. M. Arruda, S. Cowin, J. Dumais, A. Goriely, G. A. Holzapfel, J. D. Humphrey, R. Kemkemer, E. Kuhl *et al.*, *Journal of the Mechanics and Physics of Solids*, 2011, **59**, 863–883.

33 A. Abhilash, B. M. Baker, B. Trappmann, C. S. Chen and V. B. Shenoy, *Biophysical journal*, 2014, **107**, 1829–1840.

34 E. Ban, H. Wang, J. M. Franklin, J. T. Liphardt, P. A. Janmey and V. B. Shenoy, *Proceedings of the National Academy of Sciences*, 2019, **116**, 6790–6799.

35 M. Bacca, O. A. Saleh and R. M. McMeeking, *Soft matter*, 2019, **15**, 4467–4475.

36 E. Mailand, B. Li, J. Eyckmans, N. Bouklas and M. S. Sakar, *Biophysical journal*, 2019, **117**, 975–986.

37 A. V. Hill, *Proceedings of the Royal Society of London. Series B-Biological Sciences*, 1938, **126**, 136–195.

38 D.-H. Kim, P. K. Wong, J. Park, A. Levchenko and Y. Sun, *Annual review of biomedical engineering*, 2009, **11**, 203–233.

39 J. Eyckmans and C. S. Chen, *J Cell Sci*, 2017, **130**, 63–70.

40 B. A. Nerger, M. J. Siedlik and C. M. Nelson, *Cellular and molecular life sciences*, 2017, **74**, 1819–1834.

41 W. R. Legant, A. Pathak, M. T. Yang, V. S. Deshpande, R. M. McMeeking and C. S. Chen, *Proceedings of the National Academy of Sciences*, 2009, **106**, 10097–10102.

42 E. Boghaert, J. P. Gleghorn, K. Lee, N. Gjorevski, D. C. Radisky and C. M. Nelson, *Proceedings of the National Academy of Sciences*, 2012, **109**, 19632–19637.

43 H. Wang, A. A. Svoronos, T. Boudou, M. S. Sakar, J. Y. Schell, J. R. Morgan, C. S. Chen and V. B. Shenoy, *Proceedings of the National Academy of Sciences*, 2013, **110**, 20923–20928.

44 A. S. Liu, H. Wang, C. R. Copeland, C. S. Chen, V. B. Shenoy and D. H. Reich, *Scientific reports*, 2016, **6**, 1–10.

45 M. S. Sakar, J. Eyckmans, R. Pieters, D. Eberli, B. J. Nelson and C. S. Chen, *Nature communications*, 2016, **7**, 11036.

46 C.-Y. Hui, T. Liu, T. Salez, E. Raphael and A. Jagota, *Proceedings of the Royal Society A: Mathematical, Physical and Engineering Sciences*, 2015, **471**, 20140727.

47 J. Bico, É. Reyssat and B. Roman, *Annual Review of Fluid Mechanics*, 2018, **50**, 629–659.

48 R. W. Style, A. Jagota, C.-Y. Hui and E. R. Dufresne, *Annual Review of Condensed Matter Physics*, 2017, **8**, 99–118.

49 P. Steinmann, *Journal of the Mechanics and Physics of Solids*, 2008, **56**, 772–800.

50 D. L. Henann and K. Bertoldi, *Soft Matter*, 2014, **10**, 709–717.

51 Z. Liu, A. Jagota and C.-Y. Hui, *Soft Matter*, 2020, **16**, 6875–6889.

52 A. Javili, A. McBride, P. Steinmann and B. Reddy, *Computational Mechanics*, 2014, **54**, 745–762.

53 A. Javili and P. Steinmann, *Computer Methods in Applied Mechanics and Engineering*, 2010, **199**, 755–765.

54 S. Mora, C. Maurini, T. Phou, J.-M. Fromental, B. Audoly and Y. Pomeau, *Physical review letters*, 2013, **111**, 114301.

55 I. Ang, Z. Liu, J. Kim, C.-Y. Hui and N. Bouklas, *Journal of the Mechanics and Physics of Solids*, 2020, 104132.

56 W. R. Legant, C. S. Chen and V. Vogel, *Integrative Biology*, 2012, **4**, 1164–1174.

57 J. Foolen, J.-Y. Shiu, M. Mitsi, Y. Zhang, C. S. Chen and V. Vogel, *PloS one*, 2016, **11**, e0160369.

58 A. E. Green and W. Zerna, *Theoretical elasticity*, Courier Corporation, 1992.

59 N. Simha and K. Bhattacharya, *Journal of the Mechanics and Physics of Solids*, 1998, **46**, 2323–2359.

60 M. E. Gurtin and A. I. Murdoch, *Archive for rational mechanics and analysis*, 1975, **57**, 291–323.

61 P. Flory, *Transactions of the Faraday Society*, 1961, **57**, 829–838.

62 R. Ogden, *Journal of the Mechanics and Physics of Solids*, 1978, **26**, 37–57.

63 G. A. Holzapfel, T. C. Gasser and R. W. Ogden, *Journal of elasticity and the physical science of solids*, 2000, **61**, 1–48.

64 R. W. Ogden, *Non-linear elastic deformations*, Courier Corporation, 1997.

65 G. A. Holzapfel, *Nonlinear solid mechanics II*, John Wiley & Sons, Inc., 2000.

66 P. Saksono and D. Perić, *Computational Mechanics*, 2006, **38**,

265–281.
67 N. Bouklas, M. S. Sakar and W. Curtin, *ZAMM-Journal of Applied Mathematics and Mechanics/Zeitschrift für Angewandte Mathematik und Mechanik*, 2018, **98**, 1754–1770.
68 B. D. Coleman and M. E. Gurtin, *The Journal of Chemical Physics*, 1967, **47**, 597–613.
69 B. D. Coleman and W. Noll, *The Foundations of Mechanics and Thermodynamics*, Springer, 1974, pp. 145–156.
70 T. J. Hughes and K. S. Pister, *Computers & Structures*, 1978, **8**, 391–397.
71 T. J. Hughes, *The finite element method: linear static and dynamic finite element analysis*, Courier Corporation, 2012.
72 A. Logg, K.-A. Mardal, G. N. Wells *et al.*, *Automated Solution of Differential Equations by the Finite Element Method*, Springer, 2012.
73 M. S. Alnæs, J. Blechta, J. Hake, A. Johansson, B. Kehlet, A. Logg, C. Richardson, J. Ring, M. E. Rognes and G. N. Wells, *Archive of Numerical Software*, 2015, **3**, year.
74 S. Balay, S. Abhyankar, M. Adams, J. Brown, P. Brune, K. Buschelman, L. Dalcin, A. Dener, V. Eijkhout, W. Gropp *et al.*, 2019.
75 Y. Shi, J. Yao, G. Xu and L. A. Taber, *Journal of biomechanical engineering*, 2014, **136**, year.
76 E. A. Zamir and L. A. Taber, *J. Biomech. Eng.*, 2004, **126**, 823–830.
77 R. Zhao, C. S. Chen and D. H. Reich, *Biomaterials*, 2014, **35**, 5056–5064.
78 T. Wakatsuki, M. S. Kolodney, G. I. Zahalak and E. L. Elson, *Biophysical journal*, 2000, **79**, 2353–2368.
79 R. Zhao, T. Boudou, W.-G. Wang, C. S. Chen and D. H. Reich, *Advanced materials*, 2013, **25**, 1699–1705.
80 B. Kalman, C. Picart and T. Boudou, *Biomedical microdevices*, 2016, **18**, 43.
81 M. S. Hall, F. Alisafaei, E. Ban, X. Feng, C.-Y. Hui, V. B. Shenoy and M. Wu, *Proceedings of the National Academy of Sciences*, 2016, **113**, 14043–14048.